WEP Warwick Evans Publishing

International Journal of Mechanical and Electrical Engineering

ISSN: 3005-9615 (Print), ISSN: 3005-7132 (Online) | Volume 8, Number 5, Year 2026
DOI: https://doi.org/10.62051/ijmee.v8n5.01
Journal homepage: https://wepub.org/index.php/IJMEE/index

Study on Perforation Weakening Mechanism of N80 Coiled Tubing and Tool Geometry Optimization

Guofeng Hai, Wei Li

School of Mechanical Engineering, Southwest Petroleum University, Chengdu, Sichuan 610500, China

ABSTRACT

Coiled tubing fishing operation is a major technical challenge in petroleum engineering. Especially for high-strength materials such as N80, conventional direct pulling is often limited by the bearing capacity limit of the tubing. In this study, an innovative fishing process combining perforation weakening and axial fracture is proposed. Based on the finite element method of ANSYS software, the influence of tool geometry on perforation load and residual strength of tubing string is systematically investigated. The explicit dynamics method is adopted to simulate the dynamic process of the punch piercing the pipe wall and fracturing the tubing. Meanwhile, the Johnson-Cook damage model is introduced to characterize the failure behavior of N80 material under complex stress triaxiality. The results show that compared with the circular cutter head, the optimized diamond cutter head reduces the piercing load by approximately 45.3% and the fracture load by about 23%, and induces obvious stress concentration zones on the pipe wall. This research provides a theoretical basis for the design of downhole perforation fishing tools.

KEYWORDS

Coiled Tubing; Perforation Fishing; Cutter Design; Weakening Mechanism; ANSYS Explicit Dynamics.

1. INTRODUCTION

With the continuous growth in global demand for oil and gas resources, the focus of hydrocarbon exploration and development is shifting toward deeper formations, high-temperature and high-pressure (HTHP) conditions, and highly deviated wellbores. Against this background, coiled tubing (CT) technology has become a core facility in drilling, completion and workover operations due to its outstanding advantages such as high operational efficiency, strong flexibility and low cost [1,3]. However, increasingly harsh downhole environments pose severe challenges to the structural integrity of CT strings. During complex field operations, pipe sticking accidents frequently occur due to sand burial, scale deposition and wellbore instability, which seriously restrict production efficiency and greatly increase operational risks [4,6]. For such stuck pipe accidents, conventional disposal methods mainly rely on surface lifting equipment to apply overpull tension. Nevertheless, when dealing with high-strength tubing such as N80, limited by its extremely high ultimate strength, the conventional pulling method often fails because the required load exceeds the equipment limit or causes large-scale damage to the tubing string [7,8].

To improve the reliability of downhole operations, scholars worldwide have conducted extensive research on the mechanical behavior and fishing technology of coiled tubing. In terms of mechanical modeling, Liu established a mathematical model of CT under multi-load conditions based on classical mechanics theory, and verified the feasibility of finite element models in predicting ultimate bearing

capacity through experimental tests[9]. In the field of downhole monitoring and sensing, Vera adopted continuously powered sensors to realize accurate measurement of key parameters such as force, torque and pressure, which significantly improved the simulation accuracy of complex downhole environments[10]. Correa acquired real-time downhole parameters through TCT subassemblies, providing decision support for the successful recovery of downhole fish. In terms of tool development and process optimization[11], Aibaibu developed a modular fishing tool integrated with fish top detection and shearing functions[12]. Allegretti proposed an innovative fishing method that anchors the CT string and performs cutting above the free point[13]. Hassig Fonseca summarized a standard workflow covering pressure control, free point evaluation and stuck pipe release and recovery[14].

Although previous studies have achieved fruitful outcomes in fishing methods, most existing research focuses on avoiding structural failure to extend the service life of tubing strings. For extreme working conditions where high-strength N80 coiled tubing is severely stuck and cannot be pulled out, there is still a lack of systematic theoretical support for realizing targeted structural weakening through active intervention.

Therefore, this paper proposes an innovative fishing process combining perforation weakening and axial tensile fracture. Adopting a combined method of theoretical derivation, numerical simulation and experimental analysis, this study addresses the large deformation and contact nonlinearity during the perforation process via explicit dynamic simulation. The Johnson-Cook damage model is employed to characterize the failure behavior of N80 steel under complex stress triaxiality. By quantifying the influence law of cutter geometric parameters on piercing resistance, this paper aims to provide theoretical guidance for the optimal design of fishing tools, and ultimately develop a low-load and high-efficiency structural scheme for perforation tools, so as to offer a technical reference for field downhole fishing operations.

2. THEORETICAL MODEL OF PERFORATION WEAKENING

To investigate the local failure behavior of N80 coiled tubing under the "perforation weakening + axial tensile fracture" process, a theoretical analysis framework for the perforation weakening process is established based on the stress concentration theory of perforated structures, combined with the curvature characteristics of coiled tubing and the dynamic plastic damage model. It should be noted that the perforation process involves large plastic deformation, contact nonlinearity and material damage evolution, which cannot be strictly solved by the classical elastic theory. Therefore, the introduced stress concentration theory of perforated structures in this chapter is mainly adopted to reveal the influence law of different hole shapes on stress distribution and weakening tendency, and provides a theoretical foundation for the subsequent explicit dynamic finite element analysis.

2.1. Stress Concentration Theory of Perforated Tubing String

Under the action of axial tensile load, local stress concentration occurs in the perforated region of coiled tubing. To analyze the influence of hole geometry on local stress distribution, the perforated section can be simplified as a cylindrical shell structure with a central circular hole[15]. As shown in Figure 1, according to Kirsch's theory [16], in the local polar coordinate system(r, θ), let the far-field axial tensile stress be σ_∞ and the hole radius be a. The analytical expressions of stress components in each strain zone around the hole are given as follows:

(1) Radial stress formula:

$$\sigma_r = \frac{\sigma_\infty}{2}\left(1 - \frac{a^2}{r^2}\right) + \frac{\sigma_\infty}{2}\left(1 - 4\frac{a^2}{r^2} + 3\frac{a^4}{r^4}\right)\cos(2\theta) \quad (1)$$

(2) Circumferential stress formula:

$$\sigma_\theta = \frac{\sigma_\infty}{2}\left(1+\frac{a^2}{r^2}\right) - \frac{\sigma_\infty}{2}\left(1+3\frac{a^4}{r^4}\right)\cos(2\theta) \tag{2}$$

(3) Shear stress formula:

$$\tau_{r\theta} = -\frac{\sigma_\infty}{2}\left(1+2\frac{a^2}{r^2}-3\frac{a^4}{r^4}\right)\sin(2\theta) \tag{3}$$

Based on the above equations, when $r = a$ and $\theta = \pm 90^\circ$, the circumferential stress reaches its peak value $\sigma_{\theta max} = 3\sigma_\infty$. This result indicates that under axial tension, the lateral edge region of the hole is most prone to forming a local high-stress zone, which may serve as the initiation site for subsequent damage nucleation and crack propagation.

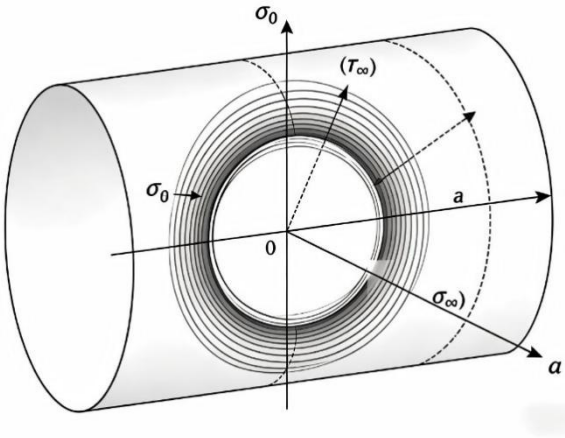

Fig 1. Schematic diagram of cylindrical shell

2.2. Equivalent Notch Model of Diamond-Shaped Hole

Compared with conventional circular perforations, diamond-shaped cutters form a more distinct geometric transition zone at the hole edge, leading to significantly intensified local stress concentration. To characterize the geometric effect at the tip of a diamond-shaped hole, its local region can be equivalent to an elliptical notch, and approximate analysis can be performed based on the Inglis notch theory. According to the Inglis formula [17], the elastic stress concentration coefficient at the end of the major axis of an elliptical hole is expressed as:

$$K_{t0} = 1 + \sqrt{\frac{2L}{\rho}} \tag{4}$$

Nomenclature:

L — Major axis length of the diamond-shaped hole, mm;

ρ— Actual chamfer radius at the tip of the diamond-shaped hole, mm.

It can be seen from the formula that the local stress concentration increases rapidly as the tip radius ρ decreases, and the stress concentration effect is further enhanced with the increase of the major axis length L. Therefore, compared with the circular hole structure, the diamond-shaped hole is more

likely to induce local plastic concentration at the sharp corner region, thereby accelerating the damage evolution.

2.3. Curvature Correction and Net Section Strength Model

Coiled tubing belongs to the thin-walled cylindrical shell structure, and bending stress exists at the hole edge in addition to plane stress. A dimensionless curvature parameter λ is introduced:

$$\lambda = \frac{L/2}{\sqrt{R_m t}} \sqrt[4]{12(1-\nu^2)} \tag{5}$$

Nomenclature:

L— Major axis length of diamond-shaped hole, mm;

Rm— Middle surface radius, mm;

t — Wall thickness of coiled tubing, mm;

v — Poisson's ratio, taken as 0.3.

Referring to the description of the curvature additional effect by the Folias factor[18], a curvature amplification factor is defined as:

$$M = \sqrt{1 + 1.25\lambda^2} \tag{6}$$

Then the comprehensive elastic stress concentration coefficient considering curvature is expressed as:

$$K_{tc} = K_{t0} \cdot M = \left(1 + \sqrt{\frac{2L}{\rho}}\right) \cdot \sqrt{1 + 1.25\lambda^2} \tag{7}$$

The Folias correction was originally proposed for cracked cylindrical shell problems. In this paper, it is adopted as an engineering approximate correction for curvature influence to qualitatively reflect the additional stress amplification effect of cylindrical shell structures compared with flat plate structures.

In addition to local stress concentration, perforation directly weakens the effective load-bearing cross-section of the tubing string. Under axial tension conditions, the residual bearing capacity of the weakened tubing is closely related to the net cross-sectional area. Accordingly, an equivalent net cross-sectional area model is introduced:

$$A_{net} = \pi(D - t)t - n \cdot W_{\max} \cdot t_{eff} \tag{8}$$

Nomenclature:

D — Outer diameter of coiled tubing, mm;

t — Wall thickness of tubing, mm;

n — Number of perforations on the same cross-section;

Wmax — Maximum projected width perpendicular to the tensile direction, mm;

t_{eff}— Equivalent load-bearing wall thickness, mm.

Determination of t_{eff} (depending on draft angle θ and hole geometry):

$$t_{eff} = t - \frac{W_{\max}}{2} \cdot \tan\theta \ (\theta \leq 10°) \tag{9}$$

2.4. Tensile Fracture Load Prediction Model Based on Finite Element Calibration

Since the classical elastic theory is difficult to characterize the large plastic deformation, material strain hardening and damage evolution behavior during the perforation process, this paper further combines finite element simulation results to realize the engineering characterization of the tensile fracture load of the weakened tubing string. A comprehensive strength degradation coefficient ζ is defined as:

$$\zeta = \frac{1}{1 + \alpha(K_{tc} - 1)^{\beta}} \tag{10}$$

Then the ultimate tensile fracture load of the weakened tubing string is:

$$P_{\max} = \sigma_b \cdot A_{net} \cdot \zeta \tag{11}$$

Nomenclature:

σ_b — Ultimate tensile strength of N80 material, MPa;

$\alpha\beta$— Fitting parameters, denoting the material plasticity sensitivity coefficient and geometric evolution exponent, respectively.

Summary of Final Formulas:

$$P_{\max} = \sigma_b \cdot \left[\pi(D - t)t - nW_{\max}t_{eff}\right] \cdot \frac{1}{1 + \alpha\left[\left(1 + \sqrt{\frac{2L}{\rho}}\right) \cdot \sqrt{1 + 1.25\lambda^2} - 1\right]^{\beta}} \tag{12}$$

This model is not a rigorous theoretical analytical model, but an engineering prediction relationship established based on finite element results, which is used to reflect the influence trend of hole geometry variation on the residual bearing capacity.

3. MATERIAL CONSTITUTIVE MODEL AND PERFORATION-TENSILE FRACTURE SIMULATION

3.1. Johnson-Cook Constitutive and Damage Model

The N80 coiled tubing is subjected to various complex loads during downhole operations, including axial tension, torsional shear, radial compression, and other loading forms. When the cutter performs perforation on the tubing, the local region of the tubing undergoes significant plastic deformation accompanied by severe stress concentration under the action of the cutter. To accurately simulate such complex nonlinear mechanical behavior, the Johnson-Cook[19] plastic hardening model is adopted to describe the constitutive relation of metallic materials under dynamic loading [20]. This model simultaneously takes into account the effects of strain hardening, strain rate sensitivity, and

thermal softening, and is suitable for characterizing the mechanical behavior of metallic materials under large deformation and high strain rate conditions. Its mathematical expression is given as:

$$\sigma_{eq} = [A + B(\varepsilon_p^{eff})^n][1 + C\ln(\varepsilon_p^*)][1 - (T^*)^m] \tag{13}$$

Nomenclature:

σ_{eq} — Equivalent stress, MPa;

ε_p^{eff} — Effective equivalent plastic strain;

ε_p^* — Dimensionless plastic strain rate;

T^* — Dimensionless temperature parameter.

There are five material constants in the model: A is the yield strength, B is the strain hardening modulus, n is the hardening exponent, C is the strain rate sensitivity coefficient, and m is the thermal softening exponent. By consulting relevant literature, the Johnson-Cook model parameters of N80 coiled tubing material were obtained [21], as listed in Table 1.

Table 1. Johnson-Cook model parameters of N80 coiled tubing

Parameter	A	B	n	C	m
value	496 MPa	434 MPa	0.307	0.015	0.804

Damage Evolution Criterion Based on Stress Triaxiality

Stress triaxiality is defined as the ratio of hydrostatic pressure to equivalent stress, which serves as a crucial index to characterize the stress state. During the perforation process, the stress state within the cutter action zone is highly complex, including a compression region with high hydrostatic pressure and a tension region with negative triaxiality. Different stress triaxiality values correspond to distinct failure modes: high positive triaxiality generally leads to ductile failure, while negative triaxiality tends to induce shear failure.

The mathematical definition of stress triaxiality is expressed as:

$$\eta = \frac{\sigma_m}{\sigma_{eq}} = \frac{(\sigma_1 + \sigma_2 + \sigma_3)/3}{\sqrt{\frac{3}{2}[(\sigma_1 - \sigma_2)^2 + (\sigma_2 - \sigma_3)^2 + (\sigma_3 - \sigma_1)^2]^{1/2}}} \tag{14}$$

Nomenclature:

σ_m — Hydrostatic pressure, MPa;

σ_{eq} — von Mises equivalent stress, MPa;

$\sigma_1, \sigma_2, \sigma_3$ — Principal stress components, MPa.

The Johnson-Cook damage model based on stress triaxiality takes the influence of stress state on material failure strain into account, and the failure strain can be expressed as:

$$\varepsilon_f = [D_1 + D_2\exp(D_3\eta)]\left[1 + D_4\ln\left(\dot{\varepsilon}^*\right)\right][1 + D_5T^*] \tag{15}$$

D_1 to D_5 are damage parameters, which need to be determined by failure tests under different stress states. The cumulative damage criterion is adopted to describe the damage evolution process, and the evolution equation of the damage variable D is expressed as:

$$\frac{\partial D}{\partial \varepsilon_p^{eff}} = \frac{1}{\varepsilon_f\left(\eta, \dot{\varepsilon}^*, T^*\right)} \tag{16}$$

When the damage variable D reaches the critical value of 1, material failure occurs. The specific parameters are listed in Table 2.

Table 2. Damage evolution model parameters of N80 coiled tubing

Parameter	D_1	D_2	D_3	D_4	D_5
value	0.06	3.31	-1.96	0.0018	0.58

The parameter D_1 represents the basic ductility of the material under uniaxial tension; D_2 and D_3 jointly characterize the influence of stress triaxiality on the failure strain; D_4 denotes the effect of strain rate on damage development, while D_5 reflects the influence of temperature.

3.2. Establishment of Finite Element Model

The explicit dynamic simulation method performs well in solving problems involving high strain rate, large deformation [22]and complex contact behaviors, and has become the mainstream approach for investigating the perforation and fishing process. Taking N80 coiled tubing as the research object, a three-dimensional nonlinear finite element model for the tubing perforation process is established via the explicit dynamic module in this study. Considering the symmetry of geometric configuration and load distribution, as shown in Figure 2, a 1/4 symmetric model is established for simplified calculation. On the premise of ensuring the circumferential constraint stiffness consistent with the full model, the computational scale is effectively reduced. A comparative analysis between the quarter model and the full model is conducted.

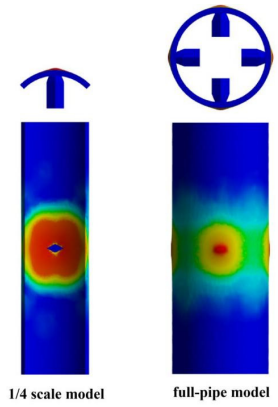

Fig 2. Comparison diagram of 1/4 pipe and full pipe

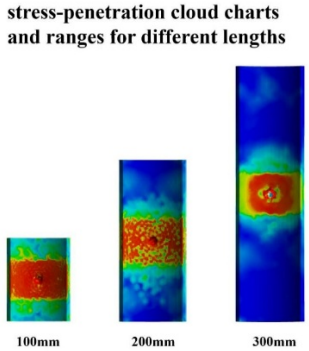

Fig 3. Comparison Diagram of Simulations with Different Lengths

The geometric structures of the tubing and cutter are modeled using SolidWorks and then imported into Workbench for numerical analysis. A standard N80 tubing with an outer radius of 57.15 mm and a wall thickness of 6.35 mm is adopted. As shown in Figure 3, through simulation comparison of different axial lengths of the tubing string, the axial length is determined as 300 mm. This length is larger than the characteristic size of the perforation affected zone, which can effectively eliminate the non-physical stiffness strengthening effect induced by end constraints on the stamping central region.

In this work, the coiled tubing adopts N80 carbon steel conforming to the API 5CT standard, which possesses excellent comprehensive mechanical properties. Considering the high stress state during perforation, precipitation-strengthened GH4169 superalloy is selected for the cutter [23]. This material maintains high hardness and simultaneously exhibits outstanding fatigue resistance. The mechanical constitutive parameters of the two materials are listed in Table 3.

Table 3. Mechanical property parameters of materials

Material	Density(kg/m)	Young's Modulus (GPa)	Poisson's Ratio	Yield Strength (MPa)	Tensile Strength (MPa)
N80	7850	206	0.3	552	680
GH4169	8240	200	0.3	1035	1275

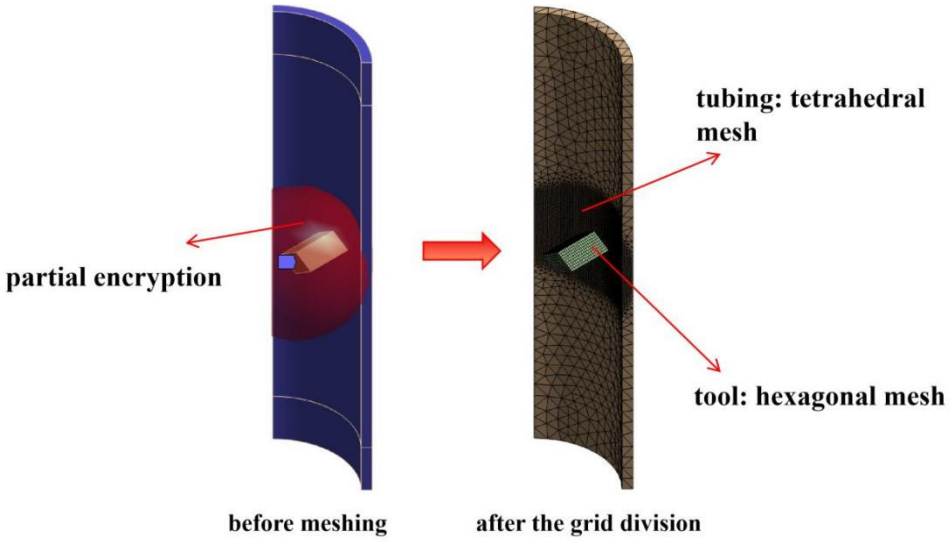

Fig 4. Comparison of Before and After Mesh Generation

In terms of preprocessing, global mesh control is first implemented for the model with an overall mesh size set to 8 mm. A local mesh refinement strategy within the influence range is adopted: the tubing is discretized with tetrahedral meshes, and the contact area between the tubing and the cutter is locally refined; the cutter is meshed with hexahedral elements, with further refinement applied to the contact surface. To improve simulation accuracy, the mesh size in the contact region between the cutter and tubing is controlled within 0.5 mm, while the mesh size gradually transitions to 2 mm in regions far from the contact zone, as shown in Figure 4. In the explicit dynamic framework, the body interaction algorithm and penalty function method are adopted for contact definition to establish master-slave contact pairs. The normal contact stiffness factor is set to 0.1 to suppress numerical oscillation. The friction behavior follows Coulomb's law with a friction coefficient of 0.1, and self-contact is activated simultaneously to simulate the secondary collision between the flared tube wall and the cutter. Regarding boundary conditions, symmetric constraints are applied on the two cutting planes of the 1/4 symmetric model to restrict normal displacement and in-plane shear stress. The

lower end of the tubing is imposed with a flexible remote displacement constraint, which only locks the axial translation and allows radial Poisson contraction, thereby eliminating false stress concentration induced by rigid boundaries. Only the radial feed degree of freedom is reserved for the cutter. Quasi-static displacement control is adopted for loading. The cutter is driven to feed radially until complete perforation via a time-history table, followed by the application of tensile load on the tubing. The loading rate is regulated to ensure the ratio of kinetic energy to internal energy is less than 5%. Both the perforation load and residual tensile strength are obtained from the reaction force at the loading end. A smooth loading step ensures the continuity of the load–displacement curve of N80 material during the yielding and initial damage stages.

4. RESULTS AND DISCUSSION

4.1. Effects of Different Factors on Tubing Perforation Load and Residual Tensile Strength

Comparative simulation results reveal that, as shown in Figure 5, the perforation load and residual tensile strength generated during tubing perforation by a rhombic cutter of the same size are evidently lower than those of the conventional cylindrical cutter. Therefore, this study mainly investigates the influences of four parameters of the rhombic cutter—major axis length under equal perimeter conditions, tool tip chamfer angle, draft length, and their combined effects—on the tubing perforation load and residual tensile strength.

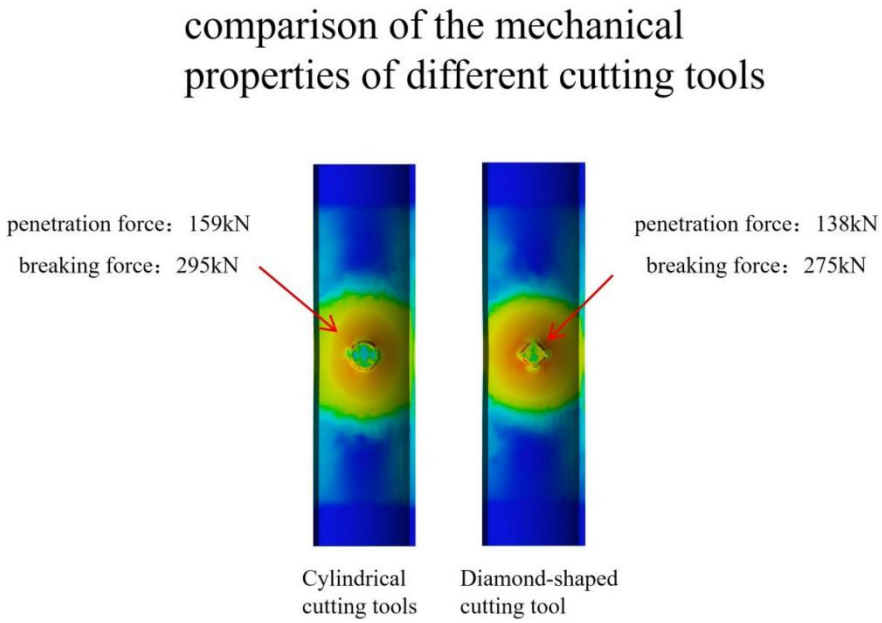

Fig 5. Comparison of Perforation and Tensile Fracture Simulations with Different Tools

Figure 6 indicates that with the increase of the major-to-minor axis ratio of the cutter, the perforation load F_p exhibits a nonlinear drag reduction trend of remaining stable initially and then dropping sharply. Within the range $L = 20{\sim}24mm$, the major-minor axis ratio changes slowly under equal perimeter with a small fluctuation amplitude; when L exceeds 26 mm, the curve slope increases significantly, showing an extremely high geometric sensitivity. Meanwhile, the residual tensile strength F_b of the weakened tubing presents a monotonically decreasing evolution with an accelerating characteristic as the major axis length L increases. The fitted curve shows an extremely high linear correlation, demonstrating that the major axis dimension is the primary dominant factor controlling the tubing weakening efficiency.

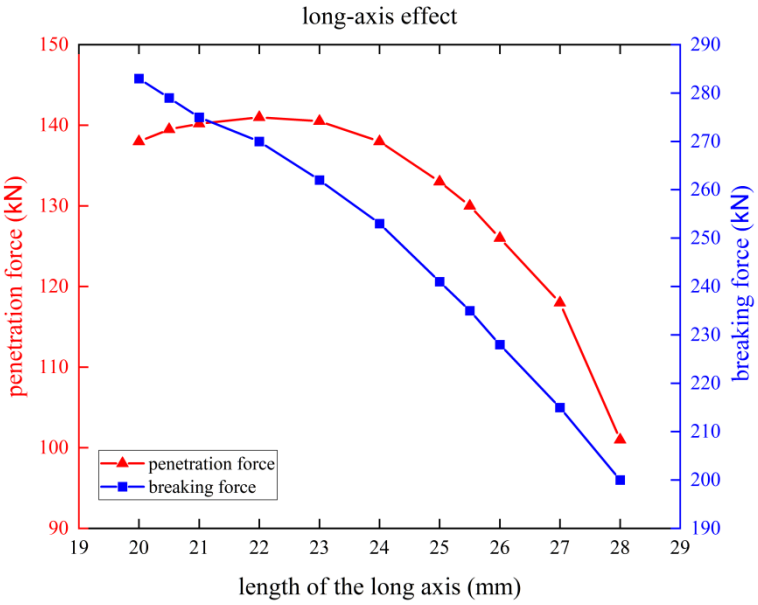

Fig 6. major axis effect

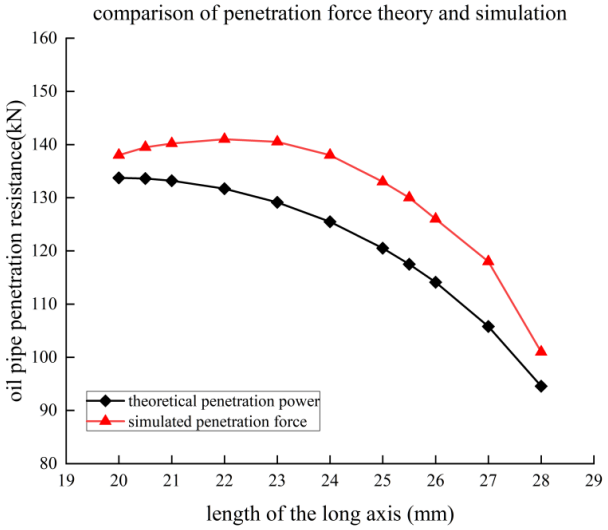

Fig 7. Comparison of Perforation Force between Theory and Simulation

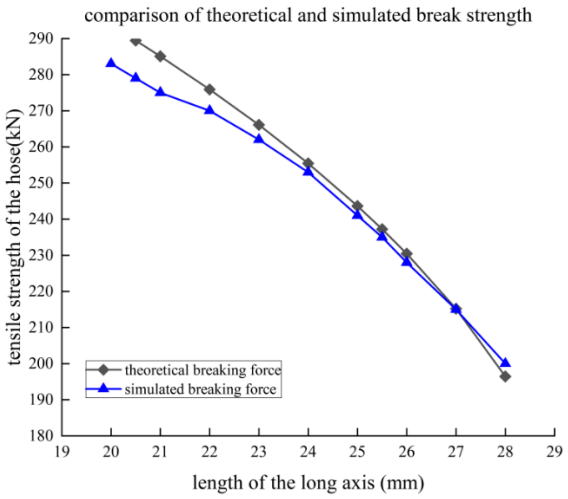

Fig 8. Comparison of break strength between Theory and Simulation

Figures 7 and 8 present the comparison curves between simulated and theoretical values under different axis ratios. It can be observed that the simulated perforation loads maintain a high logical consistency with the theoretical prediction trend, while the simulated values are generally slightly higher than the theoretical analytical results. Mechanical mechanism analysis indicates that this discrepancy mainly arises from the strain rate hardening term included in the Johnson-Cook constitutive model adopted in the explicit dynamic simulation. During transient impact, the dynamic shear strength is higher than the static theoretical value. In addition, friction dissipation at the contact interface also leads to a higher resistance in the numerical model. Despite a systematic deviation of approximately 3.4%, the two curves share highly consistent curvature, which verifies the reliability of the drag reduction mechanism. Moreover, the simulated data points of residual tensile strength almost fall exactly on the theoretical prediction line. This phenomenon illustrates that the theoretical model based on the net cross-sectional area criterion with the introduction of a stress triaxiality correction factor can preliminarily characterize the influence of stress at the rhombic hole tip on the ductility consumption of N80 steel.

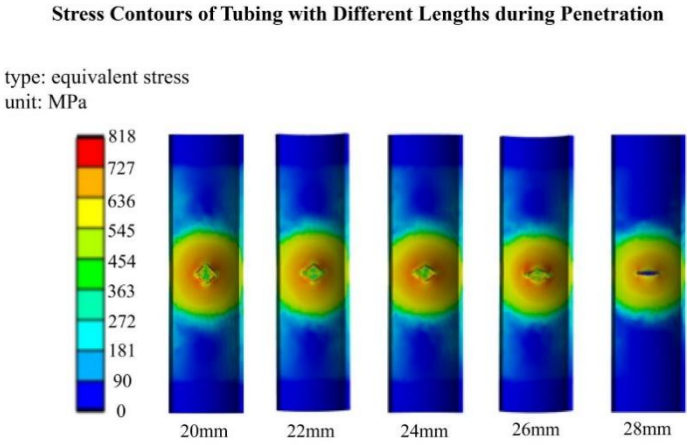

Fig 9. Comparison of Perforation Forces with Different Major Axes

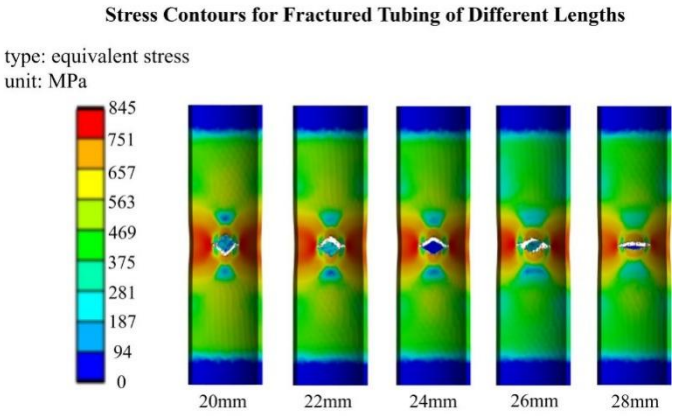

Fig 10. Comparison of Tensile Fracture Forces with Different Major Axes

Figure 9 and Figure 10 shows the simulation contours for different major axis lengths. By comparing the von Mises equivalent stress distribution contours under major axis lengths ranging from $L = 20mm$ to $L = 28mm$, distinct physical evolution laws can be identified. The contours show that as the major axis length L increases, the hole shape gradually transitions from square to flat rhombus, and the red high-stress regions become increasingly concentrated at the transverse sharp corners of the rhombus. At $L = 20mm$, the stress field distribution is relatively rounded; at $L = 28mm$, the stress gradient at the sharp corners becomes extremely steep. Such severe stress concentration is the

key factor inducing crack initiation and accounts for the substantial drop in tensile fracture lo1ad in the subsequent stage.

As shown in Figure 11, with the increase of the cutting edge chamfer radius r, the perforation load exhibits a slight nonlinear fluctuation. Within the parameter range of $0.1\sim1.2mm$, the load remains steadily between 105 kN and 112 kN. Compared with the major axis dimension, the perforation load is less sensitive to the micro-geometric features of the cutting edge. Minor changes in the edge fillet mainly affect the stress concentration degree at the initial cutting stage. A moderate chamfer can smooth the initial impact stress wave and reduce the false high load caused by numerical oscillation; an excessively large chamfer, although increasing the contact area, reduces the shear resistance per unit section through the radial extrusion effect, resulting in load fluctuation within a narrow range.

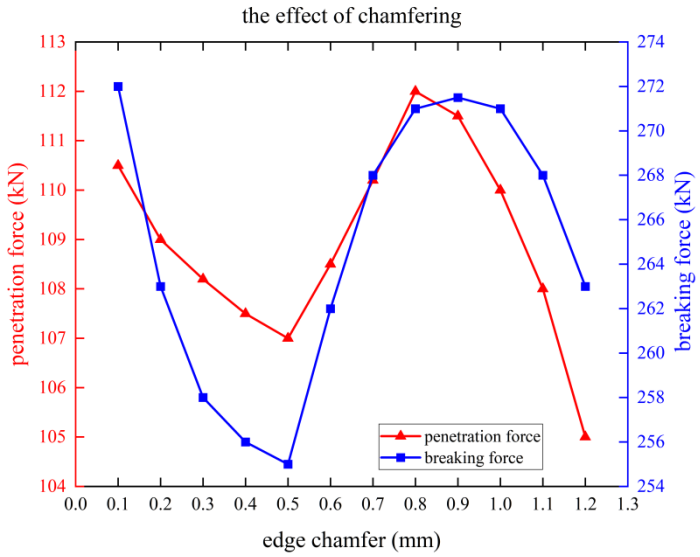

Fig 11. The effect of chamfcring

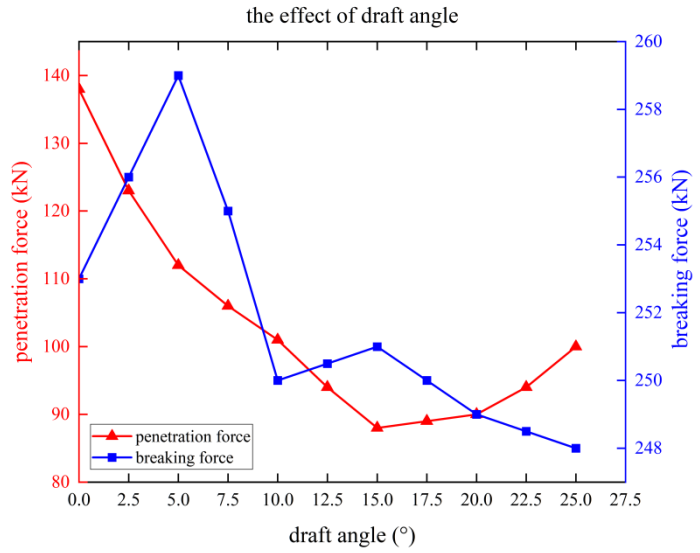

Fig 12. The effect of draft angle

As shown in Figure 12, as the draft angle increases gradually from 0°, the perforation load follows a nonlinear evolution trend of decreasing rapidly first and then rebounding slightly. The curve enters a low-level plateau within the range of 15°~20°. When the draft angle rises from 0° to near the optimal value, the peak perforation load drops from 138 kN to approximately 88 kN, achieving a maximum drag reduction rate of 36.2%. When the angle exceeds 20°, the load rebounds slightly. The residual

tensile strength F_b of the tubing maintains a high stability with the increase of draft angle α. Although the trend line decreases slightly from 256kN to 248kN, the overall fluctuation range is extremely small, with data points closely distributed around the mean baseline. Across the entire parameter range, the average residual strength is about 251.8kN with a range of only 11kN. Compared with the strength reduction effect of the major axis size, the contribution of the draft angle to the weakening effect is relatively low.

Figure 13 shows that the perforation load F_p presents a nonlinear characteristic of decreasing first and then stabilizing with the increase of draft length H. When H is near the critical range equivalent to the tubing wall thickness, the load remains at a high level of approximately$118\sim120kN$; as H increases above 10 mm, the load drops rapidly and then tends to be stable. The most significant load reduction occurs at $H = 6\sim10mm$, where the load decreases from 118kN to about 101kN, corresponding to a drag reduction ratio of 14.4%. When H>10mm, the curve slope approaches zero, and the load stabilizes at around 100kN. The residual tensile strength F_b of the tubing exhibits a weak parabolic fluctuation with the variation of draft length H. Within the entire test range, F_b fluctuates narrowly between 247kN and 253kN, with a maximum range of only 6kN, accounting for about 2.4% of the average value. This indicates that the change in draft length has little influence on the ultimate bearing capacity of the cross section.

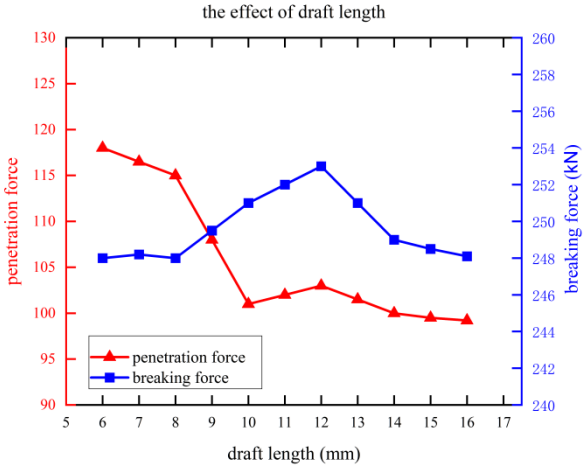

Fig 13. The effect of draft length

4.2. Evaluation of Residual Tensile Strength After Perforation

The simulation results show that the residual tensile strength F_b of the tubing string exhibits a remarkable nonlinear accelerated decline trend with the increase of the perforation major axis length L. When L=28mm, the tensile fracture load of the 1/4 symmetric model drops to a minimum value of 200kN. As L increases from 26mm to 28mm, the strength degradation efficiency per unit dimension reaches its peak.It can be observed from the von Mises stress nephograms that an extremely flat rhombic configuration induces severe stress concentration at the edge of the perforation hole. Such pronounced stress concentration effectively restrains the stable plastic flow of N80 material during the tensile stage and drives directional brittle tearing of the cross section, thereby achieving an ideal weakening effect.

Nevertheless, although L=28mm delivers the optimal weakening efficiency, the excessively large transverse span of the cutter at this dimension leads to a notable reduction in its bending section modulus. Under the strong reaction force generated during perforating high-strength N80 tubing, the internal stress of the cutter rapidly exceeds its material yield limit and induces severe plastic deformation. This load imbalance indicates that L=28mm has reached the engineering limit of the weakening tool and cannot satisfy the reliability requirement of repeated downhole operations.

According to the stress comparison of cutters with different major axis lengths (Table 4), L=26mm is the critical point that balances the fishing weakening rate and the yield strength of the tool under the working condition. Therefore, 26mm is adopted as the safety threshold in the subsequent optimization design of this paper to avoid the risk of premature cutter failure in downhole service.

Table 4. Stress values of cutters with different major axis lengths

Tool Parameters									
Major axis L(mm)	20	21	22	23	24	25	26	27	28
Axis ratio	1	1.11	1.24	1.4	1.6	1.89	2.33	3.2	7
Plastic deformation (%)	0	0	0	0.00012	0.003	0.012	0.035	0.09	0.224
Equivalent stress (Mpa)	753	782	802	830	894	960	1040	1412	1986

4.3. Mathematical Mapping Model of Tubing Load and Strength Under Variable Geometric Constraints

Since explicit dynamic simulation involves large material deformation, contact nonlinearity, and complex damage evolution processes, it exhibits strong computational nonlinearity and considerable time consumption. In the multi-parameter coupled optimization of the cutter, direct iteration by invoking the finite element solver will face the challenge of enormous computational cost. For this reason, this section adopts the response surface methodology and uses MATLAB to map discrete numerical simulation sampling points into continuous analytical expressions, so as to establish a mathematical surrogate model.

Among the numerous geometric parameters affecting the perforation weakening effect, the cutter major axis length L directly determines the physical reduction degree of the tubing cross-section and the magnitude of stress concentration. It serves as the core dominant factor that simultaneously controls the perforation dynamic load requirement and the tubing weakening efficiency. Therefore, with other parameters kept constant, the major axis length L is selected as the independent variable to conduct nonlinear regression fitting for the perforation load F_p and residual tensile strength F_b, respectively. The fitting trends and sampling point distributions are shown in Figure 14 and Figure 15.

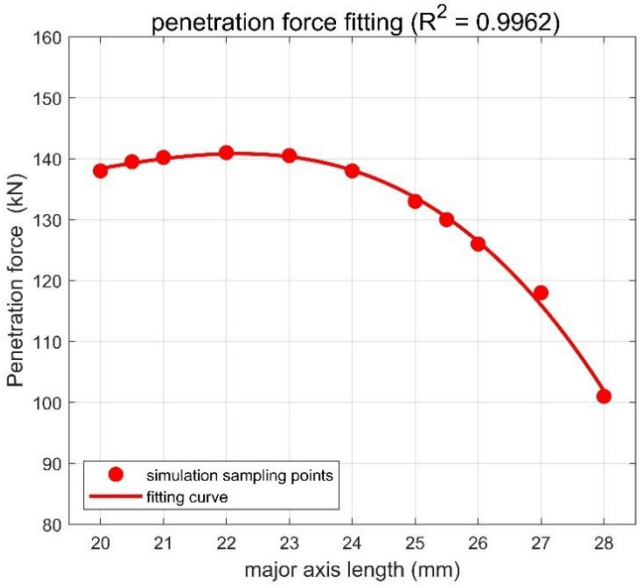

Fig 14. Penetration force fitting

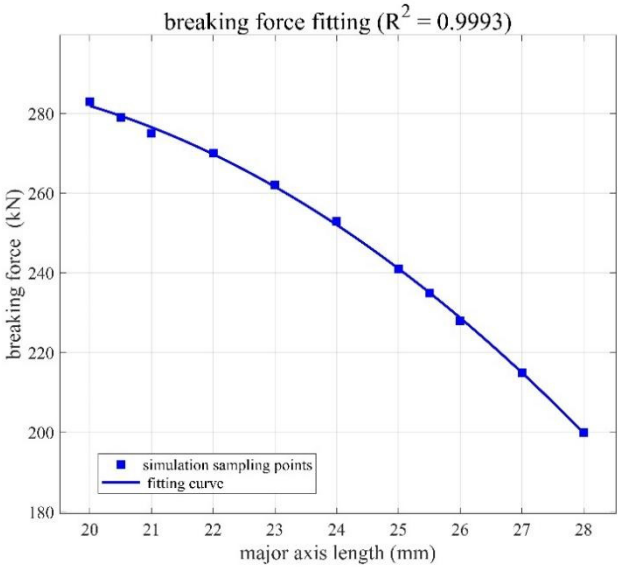

Fig 15. Breaking force fitting

(1) Prediction model of perforation load

A cubic polynomial is adopted to fit the complex load fluctuation induced by the wedging effect during the perforation process. This model can preliminarily characterize the nonlinear drop feature of load caused by the flattening of geometric configuration, and its analytical expression is given as:

$$F_p(L) = -0.0806L^3 + 4.6810L^2 - 88.6837L + 684.47 \quad (17)$$

The high-order terms in the formula reflect the instability law of N80 material induced by geometric shape in the later stage of stamping, providing a theoretical reference for the precise matching of pump pressure in downhole operations.

(2) Residual strength degradation model

The bearing capacity of the weakened tubing string presents an obvious monotonic degradation characteristic. The quadratic polynomial can well balance the calculation accuracy and formula simplicity, and its mapping relationship is as follows:

$$F_b(L) = -0.6997L^2 + 23.3251L + 95.30 \quad (18)$$

This formula quantitatively characterizes the combined effects of cross-sectional geometric weakening and stress triaxiality-induced embrittlement on N80 tubing material. Verification results show that the coefficient of determination of both models remains at a high level, indicating that the established surrogate model can well approximate the finite element response within the current parameter range and can be used for rapid prediction in subsequent optimization design.

4.4. Multi-objective Optimization of Perforation Cutter

I Overview of Optimization Strategy and Analysis Method

Although single-factor analysis reveals the influence trend of major axis length on operational load, it ignores the nonlinear interaction among parameters. Therefore, an optimization strategy combining the response surface method and multi-objective genetic algorithm is adopted in this paper.

The core logic of this method is to construct a high-precision surrogate model based on limited explicit dynamic simulation data, replace time-consuming finite element calculations in the mathematical space, and further obtain the optimal engineering scheme.

II Construction of Response Surface Surrogate Model

To establish an explicit mathematical relationship between the geometric parameters of the perforation cutter and mechanical responses, four design variables are selected in this study, including major axis length L, cutting edge fillet radius r, draft angle α, and draft length H. A second-order polynomial response surface model is established through nonlinear regression of simulation sampling points:

Perforation load prediction model:

$$F_p(L,r,\alpha,H) = \mathcal{P}_L(L) + [\mathcal{P}_r(r) - 109.5] + [\mathcal{P}_\alpha(\alpha) - 87] + [\mathcal{P}_H(H) - 87] \quad (19)$$

Residual strength prediction model:

$$F_b(L,r,\alpha,H) = \mathcal{P}_L(L) + [\mathcal{P}_r(r) - 225] + [\mathcal{P}_\alpha(\alpha) - 225] + [\mathcal{P}_H(H) - 225] \quad (20)$$

Nomenclature:

F_p, F_b: Predicted perforation load (kN) and residual tensile strength of tubing string (kN);

$P_i(x_i)$: Piecewise cubic Hermite interpolation function corresponding to the i-th geometric parameter;

109.5, 87, 225: Calibration constants of the model.

Residual analysis shows that the coefficient of determination of each model is greater than 0.98, indicating a good consistency between the fitted results and simulation data.

III Establishment of Multi-objective Optimization Mathematical Model

The optimization process aims to resolve the mechanical contradiction between reducing construction load and improving weakening efficiency.

Multi-parameter coupling optimization results of punching and fishing tools

1. Optimized Geometric Parameter combination:
   - Tool major axis length L: 26.00 mm
   - Cutting edge fillet radius r: 0.80 mm
   - Tool draft angle alpha: 15.00°
   - Tool draft length H: 11.00 mm

2. Predicted mechanical response indicataes:
   - Peak piercing load Fp: 87 kN
   - Residual tensile strength Fb: 228.00 kN

3. Compremetive energy Efficiency Optimization evaluation:
   - Reduction in piercing force compared to the original scheme: 45.3%
   - Improvement in weakening energy efficiency compared to the original scheme: 23 %

Fig 16. Optimization Result Diagram

1. Objective Functions

Objective 1: $minf_1(x) = F_p$

Objective 2: $minf_2(x) = F_b$

2. Constraint Conditions

Strength constraint:$g_1(x) = \sigma_{max} - 1200 \leq 0$

Geometric constraints:22≤L≤26; 1≤r≤1.2; 5≤α≤20; 9≤H≤14.

IV Optimization Results

As shown in figure 16,the final optimal parameter combination is determined as:

Major axis length L=26mm;Fillet radius 0.8mm;Draft angle15°;Draft length H=11mm.

Simulation verification with the optimized parameters (Table 5) shows that:

the perforation load is reduced from 159kN of the original cylindrical cutter to 87kN, with a reduction rate of 45.2%, which lowers the power requirement of the downhole hydraulic system;

the residual tensile strength of the tubing string decreases from 296kN to 228kN, and the weakening efficiency is improved by 23%.

Table 5. Comparison between optimized cutter and original cutter

Cutter type	Perforation load(kN)	Residual tensile strength(kN)	Perforation load optimization rate (%)	Residual tensile strength optimization rate (%)
Original cylindrical cutter	159	296		
Optimized diamond cutter	87	228	45.3	23

5. CONCLUSION

This paper summarizes the theoretical perforation formula and simulation process of the rhombic cutter, analyzes the variations of perforation load and residual tensile strength under different parameter conditions, and conducts formula fitting by taking the major axis length as the dominant factor affecting residual tensile strength. Finally, the optimal parameter combination is obtained through multi-objective optimization, and the main conclusions are drawn as follows:

1.Compared with the conventional circular cutter, the proposed rhombic perforation cutter can form stress concentration zones on the wall of N80 coiled tubing through directional cross-section weakening. It provides technical support for the fishing process of "perforation weakening + axial tensile fracture", and offers a feasible design idea for targeted weakening and low-load tensile fracture of stuck high-strength coiled tubing.

2.Regarding the influence law of cutter geometric parameters on perforation mechanical behavior, the major axis length acts as the core dominant factor governing the perforation load and residual strength. An increase in the major-to-minor axis ratio can reduce the perforation load. Cutting edge chamfer, draft angle and draft length mainly affect the perforation resistance and have little influence on the residual tensile strength of the tubing string. The results verify that perforation weakening is dominated by cross-section reduction and features decoupling effects of geometric parameters.

3.The cubic polynomial mapping model for perforation load and the quadratic polynomial mapping model for residual tensile strength established based on simulation sampling points can well approximate the finite element response within the current parameter range, realizing the approximate calculation of perforation mechanical properties.

4.Multi-objective global optimization effectively improves the working performance of the fishing tool. Through the collaborative optimization of the response surface method and multi-objective genetic algorithm, the optimal cutter parameter combination under the working condition is determined. After adopting the optimized scheme, the perforation load is reduced by 45.2% compared with the original scheme, which significantly lowers the power demand of the hydraulic system; meanwhile, the weakening efficiency is increased by 23%.

REFERENCES

[1] Stanley, R. K. (1998). An analysis of failures in coiled tubing. In *IADC/SPE Drilling Conference*. Society of Petroleum Engineers.

[2] McCourt, I., & Kubie, J. (2005). Limits on the penetration of coiled tubing in horizontal oil wells: Effect of the pipe geometry. *Proceedings of the Institution of Mechanical Engineers, Part C: Journal of Mechanical Engineering Science*, *219*(11), 1191–1197. https://doi.org/10.1243/095440605X32066.

[3] Wu, J., & Juvkam-Wold, H. C. (1995). Coiled tubing buckling implication in drilling and completing horizontal wells. *SPE Drill & Compl*, *10*, 16–21. https://doi.org/10.2118/26336-PA.

[4] Aadnøy, B. S., et al. (2003). Analysis of stuck pipe in deviated boreholes. *Journal of Petroleum Science and Engineering*, *37*(3–4), 195–212. https://doi.org/10.1016/S0920-4105(02)00353-4.

[5] Issa, M. A., Al-Haleem, A. A., & Mukhtar, Y. (2023). Review of the mechanisms for preventing, diagnosing and treating pipe sticking in drilling operations. *Iraqi Journal of Chemical and Petroleum Engineering*, *24*(3), 133–140. https:// doi.org/10.31699/IJCPE.2023.3.13.

[6] Burgos, R., & Mallalieu, R. (2013). Stuck coiled tubing: Addressing the risks in a complex operating environment. *Journal of Petroleum Technology*, *65*(6), 76–80. https://doi.org/10.2118/0613-0076-JPT.

[7] Xiang, G., Liu, J., & Ma, X. (2025). Technology of milling bridge plugs and field applications in shale gas horizontal wells with severe casing deformation. *Natural Gas Industry B*, *12*(1), 64–70. https://doi.org/ 10. 1016/j. ngib. 2025. 01. 005.

[8] Ding, L., Liao, T., Lian, Z., et al. (2025). Buckling failure mechanism of testing tubing string induced by expansion joint piston force in ultra-deep wells: Experimental, numerical and design optimization approaches. *Engineering Failure Analysis*, *180*, 109907. https://doi.org/10.1016/j.engfailanal.2025.109907.

[9] Shaohu, L., Hui, X., Feng, G., et al. (2017). Coiled tubing failure analysis and ultimate bearing capacity under multi-group load. *Engineering Failure Analysis*, *79*, 803–811.

[10] Vanesa, V., Carlos, T., Eduardo, D., et al. (2019, March). Successful coiled tubing fishing operation uses hybrid cable connected tools to evaluate/validate downhole data in real-time: A case study in the Eastern Foothills of Colombia. In *SPE/ICoTA Well Intervention Conference and Exhibition*, The Woodlands, Texas, USA. https://doi.org/10.2118/194260-MS.

[11] Daniel, C. P., Zhiyenaliyeva, S., & Nadirov, Z. (2022, March). Using intelligent coiled tubing for revival of a double leg well after 12 years of obstruction. In *SPE/ICoTA Well Intervention Conference and Exhibition*, The Woodlands, Texas, USA. https://doi.org/10.2118/209016-MS.

[12] Abulimit, A., Pang, D., Wang, Y., et al. (2019). Research and application of key tools for coiled tubing fishing operation. *Petroleum Drilling Techniques*, *47*(6), 89–95. https://doi.org/10.11911/syztjs.2019117.

[13] Allegretti, G., Lerose, M., Mangione, A., et al. (2022, October). A new rigless approach for fishing a stuck and parted coiled tubing in a live well. In *ADIPEC*, Abu Dhabi, UAE. https://doi.org/10.2118/211551-MS.

[14] Fonseca, S. H., Torres, R., Liu, Z., et al. (2023). Challenges and practices for recovering stuck coiled tubing pipe. *SPE Prod & Oper*, *38*, 651–665. https://doi.org/10.2118/215819-PA.

[15] Zirka, A. I., Osaulenko, L. L., & Savchenko, V. I. (1972). Stress concentrations close to circular holes in a cylindrical shell of medium thickness. *Strength of Materials*, *4*, 923–925. https://doi.org/10.1007/BF01529687.

[16] Kirsch, G. (1898). The theory of elasticity and the requirements of strength theory. *Zeitschrift des Vereins Deutscher Ingenieure*, *42*(29), 797–807.

[17] Inglis, C. E. (1913). Stresses in a plate due to the presence of cracks and sharp corners. *Transactions of the Institute of Naval Architects*, *55*, 219–241.

[18] Folias, E. S. (1965). An axial crack in a pressurized cylindrical shell. *International Journal of Fracture Mechanics*, *1*(2), 104–113.

[19] Johnson, G. R., & Cook, W. H. (1985). Fracture characteristics of three metals subjected to various strains, strain rates, temperatures and pressures. *Engineering Fracture Mechanics*, *21*(1), 31–48.

[20] Dey, S., Børvik, T., Hopperstad, O. S., et al. (2007). On the influence of constitutive relation in projectile impact of steel plates. *International Journal of Impact Engineering*, *34*(3), 464–486. https:// doi.org/ 10.1016/ j. ijimpeng. 2005. 10.003.

[21] Pang, Y. (2022). Design and research of electric cutting tool for downhole tubing [Master's thesis]. China University of Petroleum (East China). https://doi.org/10.27644/d.cnki.gsydu.2022.001143.

[22] Gao, F., Ji, C., Wu, J., et al. (2018). Experimental and numerical simulation study of perforation effect of steel pipes subjected to the impact loadings of ASC and LSC jets. *Vibroengineering PROCEDIA*, *20*, 219–224. https:// doi. org/10.21595/vp.2018.20205.

[23] Yue, S., He, Y., Song, S., et al. (2025). Parameter analysis and optimization of micro-dimple texture on turning tool surface for GH4169 nickel-based superalloy. *Diamond & Abrasives Engineering*, *45*(6), 794–806. https:// doi. org/ 10. 13394/ j.cnki.jgszz.2024.0168.